

Manuscript version: Author's Accepted Manuscript

The version presented in WRAP is the author's accepted manuscript and may differ from the published version or Version of Record.

Persistent WRAP URL:

<http://wrap.warwick.ac.uk/108277>

How to cite:

Please refer to published version for the most recent bibliographic citation information. If a published version is known of, the repository item page linked to above, will contain details on accessing it.

Copyright and reuse:

The Warwick Research Archive Portal (WRAP) makes this work by researchers of the University of Warwick available open access under the following conditions.

Copyright © and all moral rights to the version of the paper presented here belong to the individual author(s) and/or other copyright owners. To the extent reasonable and practicable the material made available in WRAP has been checked for eligibility before being made available.

Copies of full items can be used for personal research or study, educational, or not-for-profit purposes without prior permission or charge. Provided that the authors, title and full bibliographic details are credited, a hyperlink and/or URL is given for the original metadata page and the content is not changed in any way.

Publisher's statement:

Please refer to the repository item page, publisher's statement section, for further information.

For more information, please contact the WRAP Team at: wrap@warwick.ac.uk.

The origin of polarization in kilonovae and the case of the gravitational-wave counterpart AT 2017gfo

M. Bulla¹, S. Covino², K. Kyutoku^{3,4,5,6}, M. Tanaka^{7,8}, J. R. Maund⁹, F. Patat¹⁰, K. Toma^{7,11}, K. Wiersema^{12,13}, J. Bruten⁹, Z. P. Jin¹⁴ & V. Testa¹⁵

¹*Oskar Klein Centre, Department of Physics, Stockholm University, SE-106 91, Stockholm, Sweden*

²*Istituto Nazionale di Astrofisica / Brera Astronomical Observatory, via Bianchi 46, 23807 Merate (LC), Italy.*

³*Theory Center, Institute of Particle and Nuclear Studies, KEK, Tsukuba 305-0801, Japan*

⁴*Department of Particle and Nuclear Physics, the Graduate University for Advanced Studies (Sokendai), Tsukuba 305-0801, Japan*

⁵*Interdisciplinary Theoretical and Mathematical Sciences Program (iTHEMS), RIKEN, Wako, Saitama 351-0198, Japan*

⁶*Center for Gravitational Physics, Yukawa Institute for Theoretical Physics, Kyoto University, Kyoto 606-8502, Japan*

⁷*Astronomical Institute, Tohoku University, Aoba, Sendai 980-8578, Japan*

⁸*National Astronomical Observatory of Japan, National Institutes of Natural Sciences, Osawa, Mitaka, Tokyo 181-8588, Japan*

⁹*Department of Physics and Astronomy, University of Sheffield, Hicks Building, Hounsfield Road, Sheffield S3 7RH, UK*

¹⁰*European Southern Observatory, Karl-Schwarzschild-Str. 2, D-85748 Garching bei München,*

22 *Germany*

23 ¹¹*Frontier Research Institute for Interdisciplinary Sciences, Tohoku University, Sendai 980-8578,*

24 *Japan*

25 ¹²*Department of Physics & Astronomy and Leicester Institute of Space & Earth Observation, Uni-*
26 *versity of Leicester, University Road, Leicester LE1 7RH, UK*

27 ¹³*University of Warwick, Coventry, CV4 7AL, UK*

28 ¹⁴*Key Laboratory of Dark Matter and Space Astronomy, Purple Mountain Observatory, Chinese*
29 *Academy of Sciences, 210008, Nanjing, China*

30 ¹⁵*Istituto Nazionale di Astrofisica / Osservatorio Astronomico di Roma, via Frascati 33, 00078*
31 *Monte Porzio Catone, Italy*

32 **The Gravitational Wave (GW) event GW 170817 was generated by the coalescence of two**
33 **neutron stars (NS) and produced an electromagnetic transient, labelled AT 2017gfo, that was**
34 **target of a massive observational campaign. Polarimetry, a powerful diagnostic tool for prob-**
35 **ing the geometry and emission processes of unresolved sources, was obtained for this event.**
36 **The observed linear polarization was consistent with being mostly induced by intervening**
37 **dust, suggesting that the intrinsic emission was weakly polarized ($P < 0.4 - 0.5\%$). In this**
38 **paper, we present and discuss a detailed analysis of the linear polarization expected from**
39 **a merging NS binary system by means of 3D Monte Carlo radiative transfer simulations**
40 **assuming a range of possible configurations, wavelengths, epochs and viewing angles. We**
41 **find that polarization originates from the non-homogeneous opacity distribution within the**
42 **ejecta and can reach levels of $P \sim 1\%$ at early times (1–2 days after the merger) and in the**

43 **optical R band. Smaller polarization signals are expected at later epochs and/or different**
44 **wavelengths. From the viewing-angle dependence of the polarimetric signal, we constrain**
45 **the observer orientation of AT 2017gfo within $\sim 65^\circ$ from the polar direction. The detec-**
46 **tion of non-zero polarization in future events will unambiguously reveal the presence of a**
47 **lanthanide-free ejecta component and unveil its spatial and angular distribution.**

48 The discovery of GW 170817¹ and its electromagnetic counterpart AT 2017gfo has definitely
49 been an epochal event. It was generated by the merging of two NSs and produced a transient elec-
50 tromagnetic source, dubbed “kilonova” or “macronova” (hereafter referred to as kilonova). This
51 transient event was intensively followed with all the main ground-based and space-borne facilities²,
52 thus allowing us to study the evolution of the kilonova and later of the afterglow of the Gamma-
53 Ray Burst GRB 170817A^{3,4}. The optical/near-infrared observations were carried out by several
54 teams⁵⁻⁹ and delivered an almost continuous spectro-photometric and polarimetric coverage of the
55 kilonova for about a couple of weeks since discovery. Some of the main observables for this cate-
56 gory of sources were predicted a long time ago and the general agreement with the observational
57 results is truly remarkable¹⁰⁻¹⁹. Nevertheless, several details – like ejecta mass, velocity, compo-
58 sition and distribution – are still unclear despite them being crucial to e.g. turn the GW detection
59 into true rates, allow a comparison of kilonova detection limits from optical and infrared surveys
60 with GW data and compare the heavy-element yields with cosmic abundances. It is therefore
61 of paramount importance to identify new observational diagnostics able to give complementary
62 information.

63 Among these, optical and near-infrared polarimetry is of great interest since it can be sen-
64 sitive to the intrinsic geometry of the source, the composition of the emitting region material,
65 and their dynamical evolution. Some of these properties are not easily constrained by the anal-
66 ysis of (current) ordinary light curves and spectra. On the other hand, apart from a few general
67 considerations^{20,21}, there are no detailed and quantitative published studies describing the expected
68 linear polarization signatures from a kilonova produced by the merging of a NS binary system. In
69 this paper, we first discuss the theoretical scenario adopted to model the kilonova evolution from
70 about 1 day to roughly a week after the GW event. We then present linear polarization predictions
71 for different wavelengths and observer orientations, and discuss the role played by several factors
72 that cannot be unambiguously determined from other observations, such as the geometry and the
73 opening angles of the adopted ejecta components. Finally, we provide some guidelines to drive
74 future polarimetric observations of kilonovae, with or without accompanying GW data. A more
75 detailed description of the adopted models, radiative transfer simulations and results is given in the
76 Methods.

77 **Kilonova models**

78 Both the outcomes of simulations^{22–29} and the analysis of the spectro-photometric observations
79 of AT 2017gfo^{7,8} suggest that kilonovae can be interpreted as the combination of two ejecta con-
80 stituents: a first component distributed around the equatorial plane, characterized by high opacities
81 of lanthanide elements (lanthanides are a subclass of r -process elements characterized by atomic
82 number $57 \leq Z \leq 71$) and giving rise to a “faint-and-red” kilonova, and a second component in

83 the polar regions, characterized by relatively lower opacities and producing a “bright-and-blue”
 84 kilonova. Motivated by these considerations, we construct a two-component ejecta model where
 85 (i) high-opacity lanthanide-rich materials are distributed close to the equatorial plane while (ii)
 86 lanthanide-free materials with lower opacities occupy regions at higher latitudes (see Fig. 1). De-
 87 spite the general agreement between the two-component model and AT 2017gfo light curves and
 88 spectra, we note that current models^{22,24,27,30} struggle to reproduce the high velocities of the blue
 89 component and the high masses of the red component inferred for AT 2017gfo^{7,8,31–33}. However,
 90 the general polarization behaviours predicted in this work (such as the viewing angle, wavelength
 91 and time dependence of the signal) are expected to hold with using a different and/or more sophis-
 92 ticated kilonova scenario.

93 We construct our fiducial model following suggestions from both hydrodynamical simula-
 94 tions and the analysis of the spectro-photometric data of AT 2017gfo^{7,8,22–29,31–33}. Specifically, we
 95 adopt spherical ejecta with an half-opening angle of $\Phi = 30^\circ$ for the lanthanide-rich region, set
 96 the whole ejecta mass between $v_{\text{in}} = 0.05 c$ and $v_{\text{out}} = 0.3 c$ to $M_{\text{ej}} = 0.03 M_\odot$ and use a power-
 97 law density profile $\rho(v) = \rho_{\text{in}} (v/v_{\text{in}})^{-3}$, where the density at v_{in} is $\rho_{\text{in}} = 1.2 \times 10^{-12} \text{ g cm}^{-3}$.
 98 We place the photospheric surface at $v_{\text{ph}} = 0.15 c$, which at 1.5 days from the merger corre-
 99 sponds to a photospheric density of $\rho_{\text{ph}} = 5.6 \times 10^{-14} \text{ g cm}^{-3}$ and $\sim 0.01 M_\odot$ of ejecta mass
 100 above the photosphere. The ejecta are assumed to be in homologous expansion (see Methods -
 101 Our model: densities, opacities, and velocities.). Using the Monte Carlo radiative transfer code
 102 POSSIS^{34,35}, we calculate polarization levels for our fiducial model at different epochs and wave-
 103 lengths. Photon packets are created unpolarized at v_{ph} , emitted assuming constant surface bright-

104 ness and propagated throughout the whole ejecta where they can be either polarized by Thom-
105 son (electron) scattering or depolarized by bound-bound line interactions. Electron scattering and
106 wavelength-dependent bound-bound opacities are taken from numerical simulations^{15,19}, and their
107 time-dependence taken into account to investigate the polarization at different epochs (see Meth-
108 ods - Opacity calculations for lanthanide-rich and lanthanide-free ejecta for further details). Photon
109 packets escaping the ejecta are collected and used to calculate continuum polarization signals at
110 different viewing angles θ_{obs} , where $\cos \theta_{\text{obs}} = 0$ corresponds to an observer in the equatorial
111 plane.

112 **Polarization**

113 Results of the polarimetric campaign devoted to AT 2017gfo are reported in ⁵. Observations at
114 five epochs, from about 1.5 days to almost 10 days, were secured. A linear polarization of $P =$
115 $(0.50 \pm 0.07)\%$ was measured during the first epoch, while stringent upper limits were placed on
116 the following epochs, all consistent with the former measurement. The observed polarization level
117 was consistent with that shown by several stars in the field of view of the optical counterpart, and
118 therefore could be totally due to polarizing effect of dust along the line of sight³⁶.

119 In contrast to the case of supernovae (where the overall continuum polarization signal is
120 driven by the shape of the photosphere³⁷), we find that the origin of linear polarization in kilono-
121 vae mainly resides in the asymmetric distribution of lanthanide-rich material in the ejecta, resulting
122 in higher line opacities in regions closer to the equatorial plane. This leads to a net polarization sig-

123 nal since radiation from low latitudes is typically depolarized by line interactions while that from
 124 higher latitudes is more likely polarized by electron scattering interactions (see inset of Fig. 2)
 125 at favourable wavelengths and times (see below). The polarization levels predicted at rest-frame
 126 wavelengths (7000 Å, R band) and epochs (1.5 days) corresponding to the first polarimetric obser-
 127 vation of AT 2017gfo are shown in Fig. 2. Owing to the axial symmetry of the model, the linear
 128 polarization signal is carried by the Stokes parameter Q while the Stokes parameter U is null (see
 129 caption of Fig. 2 for a definition of Q and U), i.e. $P \equiv \sqrt{Q^2 + U^2} = |Q|$. The polarization signal
 130 peaks at $P = |Q| \sim 0.8\%$ for an observer in the equatorial plane ($\cos \theta_{\text{obs}} = 0$) and then decreases
 131 to smaller and smaller values moving towards the pole ($\cos \theta_{\text{obs}} = 1$) since both ejecta components
 132 are axially symmetric by construction and thus become increasingly closer to circular symmetry
 133 in projection. Our simulations show that signals of the order of 1% may therefore be detected for
 134 future kilonova events observed in the R band, at early times and at favourable viewing angles (i.e.
 135 observer orientations close to the equatorial plane). Such polarization levels are detectable for a
 136 wide range of magnitudes with current instrumentation.

137 Owing to the strong time and frequency dependence of line opacities, the polarization signal
 138 is found to vary considerably as a function of both epoch and wavelength (see Fig. 3). First, we
 139 predict a drop in polarization on short time-scales following the rapid increase of line opacities
 140 with time in both lanthanide-free and lanthanide-rich ejecta (due to a rapid temperature drop and
 141 neutralization, see Figs. 5-6). At 7000 Å, the polarization level along the equator decreases from
 142 $\sim 0.8\%$ at 1.5 days (first epoch of AT 2017gfo) to only $\sim 0.1\%$ one day after (second epoch),
 143 becoming negligible at later epochs (see Fig. 3). Secondly, the strong wavelength-dependence of

144 line opacities and the presence of two different ejecta components combine to give a maximum
145 polarization signal around 7000 Å. Moving to shorter wavelengths (5000 Å), depolarizing bound-
146 bound transitions become the dominant source of opacities in both ejecta components (see Fig. 5)
147 and thus the resulting polarization level is smaller ($P \lesssim 0.1\%$ at all viewing angles). At longer
148 wavelengths (10 000 and 15 000 Å), instead, the relative importance of electron scattering to the
149 total opacity increases in the lanthanide-rich ejecta. Compared to the case at 7000 Å, some po-
150 larizing contributions from the lanthanide-rich ejecta cancel part of the polarizing contributions
151 from the lanthanide-free ejecta, thus biasing the overall polarization signal to smaller values. As
152 a result, our simulations clearly indicate early-time spectropolarimetry in the R band as the best
153 observational strategy to detect polarization in future kilonova events.

154 **Polarization dependence on model parameters**

155 Absolute polarization levels depend on three main parameters that are uncertain and difficult to es-
156 timate from both hydrodynamical simulations and the analysis of the spectro-photometric observa-
157 tions of AT 2017gfo: the overall shape of the ejecta, the half-opening angle Φ and the photospheric
158 velocity v_{ph} .

159 The polarization signal imprinted by the global shape of the ejecta is subdominant compared
160 to that induced by the asymmetric distribution of lanthanide-rich material. Our calculations (see
161 Methods - Simulation results) indicate that ellipsoidal ejecta with axial ratio of 0.75 (i.e. semi-
162 minor axis 25 per cent shorter than semi-major axis) and lanthanide-free opacities would produce

163 only $P \lesssim 0.04\%$, a level which is much lower than those obtained from the asymmetric distribution
164 of lanthanide-rich materials ($P \sim 0.8\%$, see Fig. 2 and discussion above).

165 The impact of Φ on the polarization signal is illustrated in Fig. 4. For observers close to the
166 equatorial plane ($\cos \theta_{\text{obs}} \lesssim 0.2$), the maximum polarization signal is reached for $\Phi = 30^\circ$ when
167 the solid angle subtended by the lanthanide-rich ejecta component is 2π , i.e. half of the full solid
168 angle (see inset in Fig. 2). The partial coverage of the photosphere by the lanthanide-rich ejecta
169 is less effective in polarizing the escaping flux for both lower and higher values of Φ , therefore
170 resulting in lower signals. Nevertheless, similar polarization degrees are found for $\cos \theta_{\text{obs}} \gtrsim 0.4$
171 regardless of the value of Φ . For favourable viewing angles, comparisons between our models and
172 the combination of future spectro-photometric and polarimetric observations of kilonovae will be
173 critical to constrain the angular structures of the two ejecta components, a result which can not be
174 achieved by any other means.

175 The exact location of the photosphere (expressed in terms of the photospheric velocity v_{ph})
176 has a relatively large impact on the polarization signal. In general, moving the photosphere deeper
177 inside the ejecta leads to larger polarization since less unpolarized radiation manages to escape the
178 lanthanide-rich regions. For instance, placing the photosphere at $v_{\text{ph}} = 0.1 c$ gives a polarization
179 of $P \sim 1.9\%$ for an equatorial viewing angle, roughly twice as large compared to the fiducial
180 case with $v_{\text{ph}} = 0.15 c$. In addition to the uncertain values of v_{ph} , we note that the absolute
181 values of polarization might also be dependent on our assumption of a single photosphere. In
182 reality, the different opacities in the two ejecta components correspond to different locations of

183 the photosphere, with the lanthanide-rich region producing photons farther out compared to the
184 lanthanide-free region. We defer a more detailed treatment of the photosphere to a future study
185 (when new hydrodynamical models and observational data will likely clarify the scenario) while
186 stressing that the general polarization behaviours identified in this work are expected to hold.

187 **Constraints on the polarization of AT 2017gfo**

188 Beside predicting polarization signatures for kilonovae, our simulations are also crucial to estimate
189 the intrinsic signal in AT 2017gfo (and future events). As shown in Fig. 3, the R band polariza-
190 tion level turns out to be negligible at all viewing angles starting from ~ 2 days after the merger.
191 The signal detected after ~ 2 days in AT 2017gfo⁵ is therefore dominated by interstellar polariza-
192 tion (ISP), which we estimate to be $P_{\text{dust}} = (0.49 \pm 0.05)\%$. Reasonably assuming that the ISP
193 is the only source of polarization at late epochs and subtracting it from the one at 1.5 days (see
194 Methods - Upper limits to AT 2017gfo intrinsic polarization), a common procedure in supernova
195 polarimetry³⁷⁻³⁹, leads to an upper limit on the intrinsic polarization in AT 2017gfo of $P < 0.18\%$
196 at 95% confidence level. From the comparison between this upper limit and our model predic-
197 tions in Fig. 2, we conclude that AT 2017gfo was observed within 65 degrees from the polar axis
198 ($\cos \theta_{\text{obs}} \gtrsim 0.4$), a constraint that is less restrictive but consistent with previous estimates based on
199 spectral modelling and analysis of the associate short GRB 170817A^{7,40,41} or on the use of inde-
200 pendent distance measurements to break the inclination/distance degeneracy of the GW signal^{1,42}.
201 From Fig. 4, we note that the constraints on the inclination of AT 2017gfo are rather insensitive to
202 the specific choice of the half-opening angle of the lanthanide-rich region Φ (for $15^\circ \lesssim \Phi \lesssim 45^\circ$).

203 **Conclusions and future perspectives**

204 In this work we have, for the first time, made quantitative predictions on the expected linear po-
205 larization signature from a kilonova produced by the coalescence of a binary NS system. We
206 developed a simple model tailored to match the available observations of AT 2017gfo², the only
207 event of this category identified so far. The model does not include all the possible details that
208 are currently under discussion in the literature (e.g. the bright ultraviolet emission detected for
209 AT 2017gfo a few hours after the merger⁴³) since they are either not expected to have an important
210 effect on the derived polarization signature or their inclusion is still controversial²²⁻²⁹. Neverthe-
211 less, as far as polarization is concerned, our simple model proved to be flexible enough to allow
212 us to effectively study the role of several parameters and derive fairly solid general conclusions.
213 The model disregards the possible polarization contribution from the GRB afterglow since this is
214 negligible during the kilonova evolution⁴⁴. At the same time, however, the analysis of kilonova
215 polarization is one of the best ways to look at the structure of NS-NS mergers from the angles at
216 which we might not expect to see a GRB jet, but only the GW signal.

217 Kilonova polarization depends on the viewing angle of the source and is also time- and
218 wavelength-dependent. The maximum value should be close to the $\sim 1\%$ level, with some depen-
219 dence on (as of yet) not fully constrained model parameters such as the angular distribution of the
220 different ejecta and their expansion velocities. The polarization decreases going from equatorial to
221 polar viewing angles θ_{obs} thus providing an independent way to estimate this important parameter,
222 which strongly impacts estimates of true rates from small numbers of detections (e.g. from future

223 sources with less complete datasets than AT 2017gfo). In the case of AT 2017gfo, the viewing angle
224 turns out to be smaller than $\sim 65^\circ$, a value that is less restrictive but consistent with other indepen-
225 dent estimates from the literature^{1,7,40–42}. The polarization maximum should be detectable roughly
226 in the R band due to the particular wavelength-dependence of bound-bound opacities combined to
227 the presence of two ejecta components. No polarization is expected in the blue part of the optical
228 spectrum as far as the ejecta are composed of r-process elements, regardless of whether or not they
229 include lanthanides. Already two or three days after the GW event, the intrinsic polarization from
230 kilonovae should be virtually zero at any wavelength and viewing angle and this provides a reli-
231 able way to subtract the polarization possibly induced by dust along the line of sight. With just one
232 observed event it is hard to evaluate how general the features derived from the observations can
233 be. While a natural event-to-event variability is foreseeable, the general behaviour should anyway
234 follow the results we have described here with some effect on the absolute polarization level.

235 Polarimetry is one of the most valuable tools for uncovering the dynamics and physics of NS-
236 NS mergers. For instance, detection of non-zero polarization in future events will unambiguously
237 reveal the presence of lanthanide-free ejecta, unveil their spatial distribution – which can not be
238 investigated by any other means – and thus allow us to study the merger dynamics responsible for
239 synthesizing a diversity of r-process elements. At the same time, different results and likely higher
240 polarization degrees are expected for a kilonova generated by the merging of a BH and a NS, where
241 the lanthanide-rich dynamical ejecta are extremely deformed with an axial ratio of ~ 0.2 ^{20,21}. This
242 latter case requires a dedicated modelling and will be the target of a future study.

243 **Methods**

244 **Expectations from hydrodynamical simulations of the binary merger**

245 We adopt models of kilonova ejecta which are motivated by both hydrodynamical simulations and
246 the observed properties of the optical and near-infrared counterparts of GW170817, AT 2017gfo.

247 By hydrodynamical simulations, it is known that the ejecta from NS mergers have at least
248 two components: (1) dynamical ejecta and (2) post-merger ejecta or disk wind. The first dynamical
249 ejecta is driven by the tidal force as well as the shock heating^{22,23}. By the tidal disruption, the
250 dynamical ejecta tend to be distributed around the equatorial plane. After the dynamical ejection,
251 additional mass is ejected from the torus around the central object^{24–27}. The electron fraction Y_e
252 is an important parameter to determine the nucleosynthetic outcomes of the ejecta components.
253 Because the shock heating tends to increase the value of Y_e , the dynamical ejecta can have broad
254 distribution of Y_e . The post-merger ejecta can have higher Y_e , due to the irradiation from a neutron
255 star at the center, although the exact Y_e depends on the life time of a remnant neutron star^{28,29}. In
256 general, polar regions have higher Y_e . The mass, Y_e , and distribution of Y_e in two components may
257 vary according to the total mass and mass ratio of the merger.

258 If the ejecta include a substantial fraction of lanthanide elements, the kilonova emission
259 would be faint and red due to the high opacities of lanthanides^{13–15}. However, if the electron
260 fraction is as high as $Y_e > 0.25$, production of lanthanide elements is suppressed^{19,28,45}. Thus, the
261 ejecta that consist only of such high Y_e material produce brighter and bluer emission. Therefore, the
262 dynamical ejecta tend to give a faint, red kilonova while the post-merger ejecta are able to produce

263 a bright, blue kilonova if the effects of neutrino irradiation is strong enough. It is noted that these
264 connections may be too simple and an interplay between two components is also important⁴⁵,
265 although in the present work we preferred to keep the scenario as simple as possible without
266 introducing poorly constrained features.

267 **Parameters for GW170817**

268 Multiple ejecta components have also been confirmed in AT 2017gfo. The observed light curves
269 can be interpreted by the combination of the blue and red components^{18,46}. The mass of each
270 component is estimated to be $\sim 0.01 - 0.05 M_{\odot}$. Since the line of sight for GW170817 is $\lesssim 30^{\circ}$
271 from the pole^{1,7,40-42}, the blue component should exist in the polar direction without being fully
272 absorbed by the lanthanide-rich ejecta. This is consistent with the expectations from simulations⁴⁷.
273 However, it is not yet clear if these blue and red components can be readily interpreted as the
274 post-merger and dynamical ejecta, respectively. For example, the observed blue component has
275 a velocity of $v \sim 0.2 c$ ^{7,8,33}, which is higher than the expectation from post-merger ejecta^{24,27,30}.
276 Also, the observed red component requires a mass³¹⁻³³ larger than the typical mass from the dy-
277 namical mass ejection in the simulations²².

278 **Our model: densities, opacities and velocities**

279 Motivated by the simulations and the observations of AT 2017gfo, we adopt a simple model to
280 calculate the polarization signals. The ejecta are assumed to be in homologous (free) expansion,
281 i.e. material moving at velocity v is located at a radius $r = vt$ at any given time t . This is

282 a safe assumption for kilonovae already a few seconds after the merger. The whole ejecta have
 283 $M_{\text{ej}} = 0.03 M_{\odot}$ with a density structure of r^{-3} from $v_{\text{in}} = 0.05 c$ to $v_{\text{out}} = 0.3 c$. The slope of
 284 the density structure approximates the results of numerical simulations^{15,22}. The photosphere is
 285 placed at $v_{\text{ph}} = 0.15 c$. The ejecta are assumed to be spherical. This is not necessarily true, in
 286 particular for the dynamical ejecta, but this choice does not have a large impact on the predicted
 287 polarization because a dominant part of the signal in our models results from the partial coverage of
 288 the photosphere (see Methods - Simulation results). The whole ejecta are divided into lanthanide-
 289 rich and lanthanide-free parts depending on the angle. The separation half-opening angle is taken
 290 to be $\Phi \sim 30^\circ$ in our fiducial model. Since this angle is not well constrained by either theory or
 291 observations, we vary this parameter in our study and investigate its dependence on the predicted
 292 polarization (see Methods - Simulation results).

293 **Opacity calculations for lanthanide-rich and lanthanide-free ejecta**

294 We calculate wavelength-dependent opacities for our fiducial model using the time-dependent ra-
 295 diation transfer code^{15,19}. For lanthanide-rich ejecta as expected in the dynamical ejecta, we use
 296 the mass distribution of elements by evenly averaging the nucleosynthesis outcomes from $Y_e = 0.1$
 297 to $Y_e = 0.4$. This approximates results of numerical simulations¹⁹. Although the range includes a
 298 high Y_e , the final abundances include a large fraction of lanthanides ($\sim 9\%$ in mass fraction). In
 299 the lanthanide-rich material, most of the opacity comes from singly or doubly ionized lanthanide
 300 elements with an open f-shell. In particular, the most important bound-bound transitions are those
 301 from low-lying ($\lesssim 5 \text{ eV}$) energy levels. For the lanthanide-free ejecta, we use element abundances

302 from nucleosynthesis calculations with $Y_e = 0.3$ since the exact distribution of Y_e in the disk ejecta
303 has uncertainties. Since the radial variation of the opacities is not strong above the photosphere, we
304 simply use the opacities at the photosphere. On the other hand, the time evolution is quite strong
305 reflecting a rapid change in the ionization states, and thus we use corresponding time snapshots
306 for polarization calculations. Opacities at epochs corresponding to polarimetric observations of
307 AT 2017gfo (1.5, 2.5, 3.5 and 5.5 days) are shown in Fig. 5. In particular, bound-bound opacities
308 are averaged over a range of $\Delta\lambda = 500 \text{ \AA}$ centered at the desired wavelength (see Fig. 6). Using
309 this set of opacities, the polarization signals are calculated in a certain wavelength as a post process
310 (see Methods - Polarization simulations).

311 **Polarization simulations**

312 The three-dimensional Monte Carlo radiative transfer code POSSIS (POLarization Spectral Synthe-
313 sis In Supernovae) has been used in the past to model polarization spectra of Type Ia supernovae^{34,35}
314 and superluminous supernovae⁴⁸. Here we extend its application to predict polarization signatures
315 of kilonovae. POSSIS adopts the description of the polarization state by the Stokes parameters I , Q ,
316 U , where I is the total intensity and Q and U describe the linear polarization (the Stokes parameter
317 describing circular polarization, V , is neglected in this work). Monte Carlo photon packets are
318 created unpolarized ($Q = U = 0$) on the spherical photosphere and emitted assuming constant
319 surface brightness. Each photon packet streams freely throughout the ejecta until it undergoes
320 either a Thomson (electron) scattering or a bound-bound line transition. Bound-free and free-
321 free transitions are neglected as their opacities at epochs and wavelengths considered in this study

322 are between ~ 5 and 12 orders of magnitudes smaller than electron scattering and bound-bound
323 opacities. Thomson scattering is assumed to partially polarize the radiation, while bound-bound
324 transitions are regarded as depolarizing contributions, a computational choice usually adopted in
325 the literature⁴⁹. If an electron scattering event is selected⁵⁰, a new direction is sampled from the
326 dipole Thomson scattering matrix and the Stokes parameters I , Q and U of the packet transformed
327 accordingly^{51,52}. If a line interaction is selected, the packet is instead re-emitted in a random di-
328 rection with no polarization ($Q = U = 0$). To compute polarization signals for different viewing
329 angles, we use the “event-based technique” (EBT) described in³⁴ as this technique leads to a sub-
330 stantial reduction in the Monte Carlo noise compared to a direct-binning approach more usually
331 adopted in Monte Carlo simulations. We note that rather smooth flux spectra as those observed in
332 AT 2017gfo⁹ do not preclude rich polarization spectra⁵³. However, opacity data used here (and in
333 state-of-the-art simulations) are constructed from a few number atomic species, preventing us to
334 predict reliable polarization spectra and draw any firm conclusion about polarization connected to
335 individual line transitions.

336 **Simulation results**

337 In general, null polarization is predicted for spherical ejecta as each polarizing contribution is
338 cancelled by another contribution one quadrant away³⁷. A net polarization signal can be reflect-
339 ing either (i) an ejecta morphology departing from circular symmetry in projection or (ii) a non-
340 homogeneous asymmetric opacity distribution within the whole ejecta. To explore (i), we compute
341 polarization signatures at 7000 \AA for an ellipsoidal model with axial ratio 0.75 (in the range of the-

342 oretical expectations²²) and an homogeneous distribution of lanthanide-free opacities within the
 343 whole ejecta. When viewed from the equatorial plane, this system is associated with a polarization
 344 of $P_1 = 0.04\%$. Moving towards the pole, the ellipsoids become closer and closer to circular in
 345 projection and thus the predicted polarization levels becomes increasingly closer to zero. The pre-
 346 dicted polarization levels are almost negligible due to the combination of small electron scattering
 347 opacities and of bound-bound line opacities of the same order ($\kappa_{\text{bb}} \sim \kappa_{\text{es}} \sim 0.008 \text{ cm}^2 \text{ g}^{-1}$). For a
 348 comparison, polarization levels of $\sim 2\%$ are predicted in supernova ellipsoidal models with same
 349 axial ratio, higher electron-scattering opacities and no line opacities⁵⁴. Polarization levels similar
 350 to the one at 7000 \AA ($P \sim P_1 \sim 0.04\%$) are predicted at both $10\,000$ and $15\,000 \text{ \AA}$, while in-
 351 creasingly smaller signals are found moving to shorter wavelengths ($P \sim 0.005\%$ at 5000 \AA). To
 352 explore (ii), we calculate polarization signatures at 7000 \AA for a spherical model with lanthanide-
 353 rich opacities distributed around the equator (half-opening angle $\Phi = 30^\circ$) and lanthanide-free
 354 opacities in the rest of the ejecta (see Fig. 1). Due to the asymmetric opacity distribution shown
 355 in Fig. 5 ($\kappa_{\text{bb}}^{\text{lf}} \sim \kappa_{\text{es}}^{\text{lf}} \sim 0.008 \text{ cm}^2 \text{ g}^{-1}$ in lanthanide-free while $\kappa_{\text{bb}}^{\text{lr}} \sim 1500 \kappa_{\text{es}}^{\text{lr}} \sim 10 \text{ cm}^2 \text{ g}^{-1}$ in
 356 lanthanide-rich regions), the net polarization is no longer null as expected from spherical models
 357 but reaches values of $P_2 = 0.76\%$ 1.5 days after the merger for an equatorial orientation. Since
 358 $P_2 \gg P_1$, we conclude that the main source of polarization in kilonovae is given by the asym-
 359 metric distribution of lanthanide-rich material in the ejecta. For simplicity, the models presented
 360 in this study thus assume spherical ejecta.

361 Because radiation from the lanthanide-rich component is more likely to be depolarized by a
 362 line interaction before leaving the ejecta, most of the polarizing contributions to the signal come

363 from regions at relatively high latitudes (i.e. closer to the poles). As shown in the inset of Fig. 2,
 364 these contributions are preferentially associated with $Q < 0$ values and this explains why the
 365 models presented in this work produces negative Q polarization. Owing to the symmetry of the
 366 system about the equatorial plane, instead, $U = 0$ in all the models ($U \neq 0$ is expected for a
 367 different orientation of the equatorial-plane/merging-system on the sky). Deviations from zero in U
 368 are associated with statistical fluctuations and used as a convenient proxy for the Monte Carlo noise
 369 in Q (i.e. polarization values are quoted as $Q \pm |U|$). As shown in Fig. 2, the maximum polarization
 370 level ($Q \sim -0.8\%$) at 7000 \AA and at 1.5 days after the merger is reached for an observer in
 371 the equatorial plane ($\cos \theta_{\text{obs}} = 0$), while moving to higher latitudes leads to smaller absolute
 372 values since both the lanthanide-rich and lanthanide-free components become increasingly closer
 373 to circular symmetry in projection. As expected, $Q = 0$ for an observer along the polar direction
 374 ($\cos \theta_{\text{obs}} = 1$).

375 The wavelength-dependence of the polarization signal at 1.5 days after the merger is shown
 376 in Fig. 3. In general, moving to both shorter and longer wavelengths than 7000 \AA results into
 377 smaller polarization levels. This is due to the combination of wavelength-dependent bound-bound
 378 opacities and the presence of two ejecta components. At shorter wavelengths (5000 \AA), bound-
 379 bound transitions become the dominant opacity source in both lanthanide-free ($\kappa_{\text{bb}}^{\text{lf}} \sim 35 \kappa_{\text{es}}^{\text{lf}}$) and
 380 lanthanide-rich ($\kappa_{\text{bb}}^{\text{lr}} \sim 4200 \kappa_{\text{es}}^{\text{lr}}$) components of the ejecta. Hence, depolarizing contributions
 381 dominate the signal and the predicted polarization level is rather small for all the viewing angles
 382 ($P \lesssim 0.1\%$). Moving to longer wavelengths, instead, the relative importance of electron scattering
 383 to the total opacity increases in the lanthanide-rich ejecta ($\kappa_{\text{bb}}^{\text{lr}} \sim 1500 \kappa_{\text{es}}$ at 7000 \AA , $\kappa_{\text{bb}}^{\text{lr}} \sim 600 \kappa_{\text{es}}$

384 at 10 000 Å and $\kappa_{\text{bb}}^{\text{lr}} \sim 150 \kappa_{\text{es}}$ at 15 000 Å). As a consequence, part of the polarizing contributions
 385 from the lanthanide-free region ($Q < 0$) are cancelled by polarizing contributions one quadrant
 386 away in the lanthanide-rich region ($Q > 0$), thus biasing the overall polarization signal towards
 387 smaller values than those at 7000 Å.

388 At 7000 Å and 1.5 days after the merger, $\kappa_{\text{bb}}^{\text{lf}} \sim \kappa_{\text{es}}^{\text{lf}}$ in the lanthanide-free component while
 389 $\kappa_{\text{bb}}^{\text{lr}} \sim 1500 \kappa_{\text{es}}^{\text{lr}}$ in the lanthanide-rich component. Only one day after, bound-bound line transitions
 390 become the dominant source of opacities in all the ejecta, with $\kappa_{\text{bb}}^{\text{lf}} \sim 4 \kappa_{\text{es}}^{\text{lf}}$ and $\kappa_{\text{bb}}^{\text{lr}} \sim 2800 \kappa_{\text{es}}^{\text{lr}}$.
 391 Therefore, the rapid increase in bound-bound opacities – and the small change in electron scatter-
 392 ing opacities – in both ejecta components (see Fig. 6) causes a very fast decrease in polarization
 393 between 1.5 and 2.5 d from the merger (i.e. the first two epochs of polarimetric observations of
 394 AT 2017gfo). This is shown in Fig. 3, where the polarization along the equator at 7000 Å changes
 395 from $P \sim 0.8\%$ at 1.5 day to $P \sim 0.1\%$ at 2.5 day. Later on, the polarization signal becomes
 396 negligible ($\kappa_{\text{bb}}^{\text{lf}} \sim 400 \kappa_{\text{es}}^{\text{lf}}$ and $\kappa_{\text{bb}}^{\text{lr}} \sim 40\,000 \kappa_{\text{es}}^{\text{lr}}$ at 3.5 days). Similar time-evolution are seen at
 397 different wavelengths.

398 Polarization in our models is attributed to the partial coverage of the photosphere by the
 399 high-opacity lanthanide-rich material. The extent of the lanthanide-rich component is therefore an
 400 important parameter in setting the absolute polarization values. In particular, different values of Φ
 401 correspond to different regions of the ejecta bringing low-polarization contributions and thus they
 402 lead to different polarization signals. Fig. 4 shows polarization levels at 1.5 days for different val-
 403 ues of Φ : 15°, 22.5°, 30°, 37.5° and 45°. The maximum polarization level is reached for $\Phi = 30^\circ$
 404 since in this configuration the partial coverage of the photosphere by the lanthanide-rich ejecta cor-

405 responds to half of the full solid angle, i.e. $\Delta\Omega = 4\pi \times \sin \Phi = 2\pi$ (see inset of Fig. 2). For lower
 406 values of Φ , the partial coverage of the photosphere is smaller and positive Q contributions from
 407 regions close to the equatorial plane partially cancel the negative contribution from polar regions,
 408 thus bringing the overall polarization signal to smaller absolute values. For higher values of Φ ,
 409 instead, the partial coverage is higher, causing an increase in the contribution to the total flux of
 410 photons from the lanthanide-rich regions. Since these photon packets are preferentially unpolar-
 411 ized, the overall polarization level decreases. Nevertheless, polarization signals for $\cos \theta_{\text{obs}} \gtrsim 0.4$
 412 are predicted to be similar for all the set of Φ values investigated since at relatively high latitudes
 413 the lanthanide-rich component is deeper inside the ejecta (see Fig. 1) and contributes less to the
 414 final emitted flux. Although hydrodynamical simulations^{45,47,55,56} suggest that Φ might be in the
 415 range of 30–45 degrees, we note that larger values – not excluded *per se* – would be associated to
 416 negligible polarization signals ($P \lesssim 0.2\%$).

417 The location of the photosphere (parametrised by the photospheric velocity v_{ph}) has a rela-
 418 tively large impact on the polarization signal. In our fiducial model, with the photosphere modelled
 419 as a spherical surface at $v_{\text{ph}} = 0.15 c$, the polarization in the equatorial plane is $P \sim 0.8\%$ at
 420 7000 Å and 1.5 days after the merger. Moving the photosphere to $v_{\text{ph}} = 0.1 c$, the relative increase
 421 in optical depth to the boundary is larger in the lanthanide-rich compared to the lanthanide-free
 422 regions. This means that the contribution of the lanthanide-rich region to the total flux changes
 423 from ~ 93 per cent at $v_{\text{ph}} = 0.15 c$ to ~ 89 per cent at $v_{\text{ph}} = 0.1 c$. Because of the depolarizing
 424 contribution of the lanthanide-rich component, the decrease in flux corresponds to an increase in
 425 the overall polarization. Specifically, a polarization of $P \sim 1.9\%$ is found for the model with

426 $v_{\text{ph}} = 0.1 c$, roughly twice as large compared to the fiducial model with $v_{\text{ph}} = 0.15 c$.

427 **Comparison with previous polarimetric studies**

428 Polarization signatures for similar geometries have been predicted in previous stellar^{57,58} and
429 supernova^{34,59,60} studies. The qualitative polarization behaviours identified in these works bear
430 strong similarities to those found in our simulations. First, a polarization decrease to zero with
431 increasing inclination (see Fig. 2) is predicted by previous studies adopting similar axisymmet-
432 ric morphologies (see e.g. fig. 5b of ⁵⁸, fig. 18 of ⁶⁰ and fig. 7 of ³⁴). Moreover, the temporal
433 evolution of polarization seen in Fig. 3 is in qualitative agreement with that predicted by axisym-
434 metric supernova models although over different time-scales (see e.g. fig. 16 of ³⁴). Finally, the
435 smaller polarization levels found at 5000 compared to 7000 Å (see Fig. 3) are reminiscent of those
436 predicted in Type Ia supernova models and usually ascribed to the increasing importance of depo-
437 larizing bound-bound transitions when moving from longer to shorter optical wavelengths^{61,62}.

438 Differences in the adopted morphologies, opacities and densities make quantitative compar-
439 isons between polarization levels from our simulations and those from the literature difficult. For
440 instance, studies like ^{57,58} neglect bound-bound opacities and focus on continuum processes by
441 predicting the polarization signals as a function of the albedo $a = \kappa_{\text{es}}/\kappa_{\text{tot}} = \kappa_{\text{es}}/(\kappa_{\text{es}} + \kappa_{\text{bf}} + \kappa_{\text{ff}})$,
442 where κ_{bf} and κ_{ff} are the bound-free and free-free opacities, respectively. In contrast, bound-free
443 and free-free opacities are neglected in our simulations and the albedo computed as $\kappa_{\text{es}}/(\kappa_{\text{es}} + \kappa_{\text{bb}})$.
444 More importantly, previous studies remove photons undergoing either bound-free or free-free in-
445 teractions from the simulations. In contrast, no sink is introduced in our calculations and photons

446 undergoing bound-bound interactions are re-emitted isotropically and with no polarization. The
447 different choices in the opacity sources and treatments make a significant impact on the predicted
448 polarization levels.

449 Although a full quantitative comparison is beyond the scope of this study, we note that po-
450 larization percentages predicted here are in the same range found by previous works. For instance,
451 our simulations adopt albedo of ~ 0 and ~ 0.5 at 1.5 days and at 7000 \AA in the lanthanide-rich and
452 lanthanide-free ejecta, respectively (see Methods - Simulation results). The resulting polarization
453 level of $\sim 0.8 \%$ for an equatorial viewing angle (see Fig. 2) is within the range of $\sim 0.2 - 1.5 \%$
454 predicted by ⁵⁸ for albedo between 0.1 and 0.5 (see their fig. 5b).

455 **Upper limits to AT 2017gfo intrinsic polarization**

456 The results of the polarimetric campaign carried out for AT 2017gfo are reported in ⁵. In spite
457 of the fair signal-to-noise obtained with the observations, the main limitation to the derived upper
458 limits, $P < 0.4 - 0.5 \%$, is due to the effect of polarization induced by dust along the line of sight in
459 both our and the host galaxy³⁶. In fact, observation of stars in the field of view showed polarization
460 from virtually zero up to $\sim 0.7 \%$. The polarization derived for AT 2017gfo during the first epoch
461 (~ 1.5 days after the event) is consistent with this value, while at later epoch only upper limits were
462 obtained. Following a strategy already applied for supernova spectro-polarimetric observations
463 (e.g. ^{38,39}), it is possible to derive a much better estimate for the first epoch polarization. According
464 to the results of our analysis (see Polarization), the R band flux from the kilonova is completely non
465 polarized for any viewing direction at epochs later than 2 – 3 days, due to the high line opacity of

466 the emitting material. Therefore, by a weighted average of the results of the observations in the R
467 band at all epochs but the first we can obtain a solid estimate of the polarization induced by any dust
468 along the line of sight. Using data reported in Tables 1 and 2 in ⁵ we get $Q_{\text{dust}} = -0.0021 \pm 0.0006$
469 and $U_{\text{dust}} = 0.0044 \pm 0.0005$, corresponding to $P_{\text{dust}} = (0.49 \pm 0.05)\%$ and a position angle
470 $\chi_{\text{dust}} = (58 \pm 4)^\circ$, in fair agreement with what it was observed for the field stars⁵. By subtracting
471 the average value to Q and U obtained for the first epoch we then derive our best estimate of the
472 intrinsic polarization from AT 2017gfo: $Q = -0.0003 \pm 0.0009$ and $U = 0.0009 \pm 0.0005$, which
473 corresponds, following ⁶³, to an upper limit of $P < 0.18\%$ at 95% confidence level.

474 **Code availability.** The radiative transfer code POSSIS used in this work is not publicly avail-
475 able. Results presented in this work are available from the corresponding author upon reasonable
476 request.

- 478 1. Abbott, B. P. *et al.* GW170817: Observation of Gravitational Waves from a Binary Neutron
479 Star Inspiral. *Physical Review Letters* **119**, 161101 (2017). 1710.05832.
- 480 2. Abbott, B. P. *et al.* Multi-messenger Observations of a Binary Neutron Star Merger. *ApJ* **848**,
481 L12 (2017). 1710.05833.
- 482 3. Mooley, K. P. *et al.* Superluminal motion of a relativistic jet in the neutron star merger
483 GW170817. *ArXiv e-prints* (2018). 1806.09693.
- 484 4. Ghirlanda, G. *et al.* Re-solving the jet/cocoon riddle of the first gravitational wave with an
485 electromagnetic counterpart. *ArXiv e-prints* (2018). 1808.00469.

- 486 5. Covino, S. *et al.* The unpolarized macronova associated with the gravitational wave event GW
487 170817. *Nature Astronomy* **1**, 791–794 (2017). 1710.05849.
- 488 6. Evans, P. A. *et al.* Swift and NuSTAR observations of GW170817: Detection of a blue kilo-
489 nova. *Science* **358**, 1565–1570 (2017). 1710.05437.
- 490 7. Pian, E. *et al.* Spectroscopic identification of r-process nucleosynthesis in a double neutron-
491 star merger. *Nature* **551**, 67–70 (2017). 1710.05858.
- 492 8. Smartt, S. J. *et al.* A kilonova as the electromagnetic counterpart to a gravitational-wave
493 source. *Nature* **551**, 75–79 (2017). 1710.05841.
- 494 9. Tanvir, N. R. *et al.* The Emergence of a Lanthanide-rich Kilonova Following the Merger of
495 Two Neutron Stars. *ApJ* **848**, L27 (2017). 1710.05455.
- 496 10. Li, L.-X. & Paczyński, B. Transient Events from Neutron Star Mergers. *ApJ* **507**, L59–L62
497 (1998). astro-ph/9807272.
- 498 11. Metzger, B. D. *et al.* Electromagnetic counterparts of compact object mergers powered by the
499 radioactive decay of r-process nuclei. *MNRAS* **406**, 2650–2662 (2010). 1001.5029.
- 500 12. Roberts, L. F., Kasen, D., Lee, W. H. & Ramirez-Ruiz, E. Electromagnetic Transients Powered
501 by Nuclear Decay in the Tidal Tails of Coalescing Compact Binaries. *ApJ* **736**, L21 (2011).
502 1104.5504.
- 503 13. Kasen, D., Badnell, N. R. & Barnes, J. Opacities and Spectra of the r-process Ejecta from
504 Neutron Star Mergers. *ApJ* **774**, 25 (2013). 1303.5788.

- 505 14. Barnes, J. & Kasen, D. Effect of a High Opacity on the Light Curves of Radioactively Powered
506 Transients from Compact Object Mergers. *ApJ* **775**, 18 (2013). 1303.5787.
- 507 15. Tanaka, M. & Hotokezaka, K. Radiative Transfer Simulations of Neutron Star Merger Ejecta.
508 *ApJ* **775**, 113 (2013). 1306.3742.
- 509 16. Baiotti, L. & Rezzolla, L. Binary neutron star mergers: a review of Einstein's richest labora-
510 tory. *Reports on Progress in Physics* **80**, 096901 (2017). 1607.03540.
- 511 17. Metzger, B. D. Kilonovae. *Living Reviews in Relativity* **20**, 3 (2017). 1610.09381.
- 512 18. Tanaka, M. *et al.* Kilonova from post-merger ejecta as an optical and near-Infrared counterpart
513 of GW170817. *PASJ* **69**, 102 (2017). 1710.05850.
- 514 19. Tanaka, M. *et al.* Properties of Kilonovae from Dynamical and Post-merger Ejecta of Neutron
515 Star Mergers. *ApJ* **852**, 109 (2018). 1708.09101.
- 516 20. Kyutoku, K., Ioka, K. & Shibata, M. Anisotropic mass ejection from black hole-neutron
517 star binaries: Diversity of electromagnetic counterparts. *Phys. Rev. D* **88**, 041503 (2013).
518 1305.6309.
- 519 21. Kyutoku, K., Ioka, K., Okawa, H., Shibata, M. & Taniguchi, K. Dynamical mass ejection
520 from black hole-neutron star binaries. *Phys. Rev. D* **92**, 044028 (2015). 1502.05402.
- 521 22. Hotokezaka, K. *et al.* Mass ejection from the merger of binary neutron stars. *Phys. Rev. D* **87**,
522 024001 (2013). 1212.0905.

- 523 23. Bauswein, A., Goriely, S. & Janka, H.-T. Systematics of Dynamical Mass Ejection, Nucleo-
524 osynthesis, and Radioactively Powered Electromagnetic Signals from Neutron-star Mergers.
525 *ApJ* **773**, 78 (2013). 1302.6530.
- 526 24. Fernández, R. & Metzger, B. D. Delayed outflows from black hole accretion tori following
527 neutron star binary coalescence. *MNRAS* **435**, 502–517 (2013). 1304.6720.
- 528 25. Siegel, D. M. & Metzger, B. D. Three-Dimensional General-Relativistic Magnetohydrody-
529 namic Simulations of Remnant Accretion Disks from Neutron Star Mergers: Outflows and r
530 -Process Nucleosynthesis. *Physical Review Letters* **119**, 231102 (2017). 1705.05473.
- 531 26. Shibata, M., Kiuchi, K. & Sekiguchi, Y.-i. General relativistic viscous hydrodynamics of
532 differentially rotating neutron stars. *Phys. Rev. D* **95**, 083005 (2017). 1703.10303.
- 533 27. Fujibayashi, S., Sekiguchi, Y., Kiuchi, K. & Shibata, M. Properties of Neutrino-driven Ejecta
534 from the Remnant of Binary Neutron Star Merger : Purely Radiation Hydrodynamics Case.
535 *ArXiv e-prints* (2017). 1703.10191.
- 536 28. Metzger, B. D. & Fernández, R. Red or blue? A potential kilonova imprint of the delay
537 until black hole formation following a neutron star merger. *MNRAS* **441**, 3444–3453 (2014).
538 1402.4803.
- 539 29. Lippuner, J. *et al.* Signatures of hypermassive neutron star lifetimes on r-process nucle-
540 osynthesis in the disc ejecta from neutron star mergers. *MNRAS* **472**, 904–918 (2017).
541 1703.06216.

- 542 30. Perego, A. *et al.* Neutrino-driven winds from neutron star merger remnants. *MNRAS* **443**,
543 3134–3156 (2014). 1405.6730.
- 544 31. Chornock, R. *et al.* The Electromagnetic Counterpart of the Binary Neutron Star Merger
545 LIGO/Virgo GW170817. IV. Detection of Near-infrared Signatures of r-process Nucleosyn-
546 thesis with Gemini-South. *ApJ* **848**, L19 (2017). 1710.05454.
- 547 32. Cowperthwaite, P. S. *et al.* The Electromagnetic Counterpart of the Binary Neutron Star
548 Merger LIGO/Virgo GW170817. II. UV, Optical, and Near-infrared Light Curves and Com-
549 parison to Kilonova Models. *ApJ* **848**, L17 (2017). 1710.05840.
- 550 33. Nicholl, M. *et al.* The Electromagnetic Counterpart of the Binary Neutron Star Merger
551 LIGO/Virgo GW170817. III. Optical and UV Spectra of a Blue Kilonova from Fast Polar
552 Ejecta. *ApJ* **848**, L18 (2017). 1710.05456.
- 553 34. Bulla, M., Sim, S. A. & Kromer, M. Polarization spectral synthesis for Type Ia supernova
554 explosion models. *MNRAS* **450**, 967–981 (2015). 1503.07002.
- 555 35. Bulla, M. *Polarisation Spectral Synthesis For Type Ia Supernova Explosion Models*. Ph.D.
556 thesis, Astrophysics Research Centre, School of Mathematics and Physics, Queen’s University
557 Belfast, Belfast BT7 1NN, UK (2017).
- 558 36. Serkowski, K., Mathewson, D. S. & Ford, V. L. Wavelength dependence of interstellar polar-
559 ization and ratio of total to selective extinction. *ApJ* **196**, 261–290 (1975).
- 560 37. Wang, L. & Wheeler, J. C. Spectropolarimetry of Supernovae. *ARA&A* **46**, 433–474 (2008).
561 0811.1054.

- 562 38. Maund, J. R. *et al.* Spectropolarimetry of the Type IIb Supernova 2001ig. *ApJ* **671**, 1944–1958
563 (2007). 0709.1487.
- 564 39. Patat, F. *et al.* VLT Spectropolarimetry of the Type Ia SN 2005ke. A step towards understand-
565 ing subluminescent events. *A&A* **545**, A7 (2012). 1206.1858.
- 566 40. Troja, E. *et al.* The X-ray counterpart to the gravitational-wave event GW170817. *Nature* **551**,
567 71–74 (2017). 1710.05433.
- 568 41. Finstad, D., De, S., Brown, D. A., Berger, E. & Biwer, C. M. Measuring the viewing
569 angle of GW170817 with electromagnetic and gravitational waves. *ArXiv e-prints* (2018).
570 1804.04179.
- 571 42. Mandel, I. The Orbit of GW170817 Was Inclined by Less Than 28deg to the Line of Sight.
572 *ApJ* **853**, L12 (2018). 1712.03958.
- 573 43. Metzger, B. D., Thompson, T. A. & Quataert, E. A Magnetar Origin for the Kilonova Ejecta
574 in GW170817. *ApJ* **856**, 101 (2018). 1801.04286.
- 575 44. D’Avanzo, P. *et al.* The evolution of the X-ray afterglow emission of GW 170817 / GRB
576 170817A in XMM-Newton observations. *ArXiv e-prints* (2018). 1801.06164.
- 577 45. Kasen, D., Fernández, R. & Metzger, B. D. Kilonova light curves from the disc wind outflows
578 of compact object mergers. *MNRAS* **450**, 1777–1786 (2015). 1411.3726.

- 579 46. Kasen, D., Metzger, B., Barnes, J., Quataert, E. & Ramirez-Ruiz, E. Origin of the heavy
580 elements in binary neutron-star mergers from a gravitational-wave event. *Nature* **551**, 80–84
581 (2017). 1710.05463.
- 582 47. Shibata, M. *et al.* Modeling GW170817 based on numerical relativity and its implications.
583 *Phys. Rev. D* **96**, 123012 (2017). 1710.07579.
- 584 48. Inserra, C., Bulla, M., Sim, S. A. & Smartt, S. J. Spectropolarimetry of Superluminous Super-
585 novae: Insight into Their Geometry. *ApJ* **831**, 79 (2016). 1607.02353.
- 586 49. Jeffery, D. J. The Sobolev-P method - A generalization of the Sobolev method for the treatment
587 of the polarization state of radiation and the polarizing effect of resonance line scattering. *ApJS*
588 **71**, 951–981 (1989).
- 589 50. Mazzali, P. A. & Lucy, L. B. The application of Monte Carlo methods to the synthesis of
590 early-time supernovae spectra. *A&A* **279**, 447–456 (1993).
- 591 51. Chandrasekhar, S. *Radiative transfer* (Dover Publications, New York, 1960).
- 592 52. Code, A. D. & Whitney, B. A. Polarization from scattering in blobs. *ApJ* **441**, 400–407
593 (1995).
- 594 53. Wang, L., Wheeler, J. C. & Höflich, P. Polarimetry of the Type IA Supernova SN 1996X. *ApJ*
595 **476**, L27–L30 (1997). astro-ph/9609178.
- 596 54. Hoflich, P. Asphericity Effects in Scattering Dominated Photospheres. *A&A* **246**, 481 (1991).

- 597 55. Martin, D. *et al.* Neutrino-driven Winds in the Aftermath of a Neutron Star Merger: Nucleo-
598 osynthesis and Electromagnetic Transients. *ApJ* **813**, 2 (2015). 1506.05048.
- 599 56. Bovard, L. *et al.* r-process nucleosynthesis from matter ejected in binary neutron star mergers.
600 *Phys. Rev. D* **96**, 124005 (2017). 1709.09630.
- 601 57. Hillier, D. J. The calculation of continuum polarization due to the Rayleigh scattering phase
602 matrix in multi-scattering axisymmetric envelopes. *A&A* **289**, 492–504 (1994).
- 603 58. Wood, K., Bjorkman, J. E., Whitney, B. & Code, A. The Effect of Multiple Scattering on
604 the Polarization from Axisymmetric Circumstellar Envelopes. II. Thomson Scattering in the
605 Presence of Absorptive Opacity Sources. *ApJ* **461**, 847 (1996).
- 606 59. Kasen, D. *et al.* Analysis of the Flux and Polarization Spectra of the Type Ia Supernova
607 SN 2001el: Exploring the Geometry of the High-Velocity Ejecta. *ApJ* **593**, 788–808 (2003).
608 [astro-ph/0301312](https://arxiv.org/abs/astro-ph/0301312).
- 609 60. Dessart, L. & Hillier, D. J. Synthetic line and continuum linear-polarization signatures of
610 axisymmetric Type II supernova ejecta. *MNRAS* **415**, 3497–3519 (2011). 1104.5346.
- 611 61. Kasen, D., Nugent, P., Thomas, R. C. & Wang, L. Could There Be a Hole in Type Ia Super-
612 novae? *ApJ* **610**, 876–887 (2004). [astro-ph/0311009](https://arxiv.org/abs/astro-ph/0311009).
- 613 62. Bulla, M. *et al.* Predicting polarization signatures for double-detonation and delayed-
614 detonation models of Type Ia supernovae. *MNRAS* **462**, 1039–1056 (2016). 1607.04081.

615 63. Plaszczynski, S., Montier, L., Levrier, F. & Tristram, M. A novel estimator of the polarization
616 amplitude from normally distributed Stokes parameters. *MNRAS* **439**, 4048–4056 (2014).
617 1312.0437.

618 **Acknowledgements** The authors thank the anonymous referees for their constructive feedback which im-
619 proved this paper. M.B. acknowledges support from the Swedish Research Council (Vetenskapsrådet) and
620 the Swedish National Space Board. S.C. acknowledges support from ASI grant I/004/11/3. K.K. is sup-
621 ported by Japanese Society for the Promotion of Science (JSPS) Kakenhi Grant-in-Aid for Scientific Re-
622 search (No. JP16H06342, No. JP17H01131, No. JP18H04595). J.R.M. is supported through a Royal Society
623 University Research Fellowship. K.T. is supported by JSPS Kakenhi No. 15H05437 and No. 18H01245,
624 and also by a JST grant Buidling of Consortia for the Development of Human Resources in Science and
625 Technology. J.B. is supported by a University of Sheffield PhD studentship.

626 **Author contributions** All authors contributed to the work presented in this paper. M.B. carried out the
627 model simulations and analysis and led the writing of the manuscript. S.C. provided polarimetric data of
628 AT 2017gfo and helped with the writing. K.K. and M.T. provided theoretical insights on hydrodynamical
629 models, carried out radiative transfer calculations to estimate opacities and helped with the writing of the
630 manuscript.

631 **Competing Interests** The authors declare that they have no competing financial interests.

632 **Correspondence** Correspondence and requests for materials should be addressed to M.B. or S.C. (email:
633 mattia.bulla@fysik.su.se, stefano.covino@inaf.it).

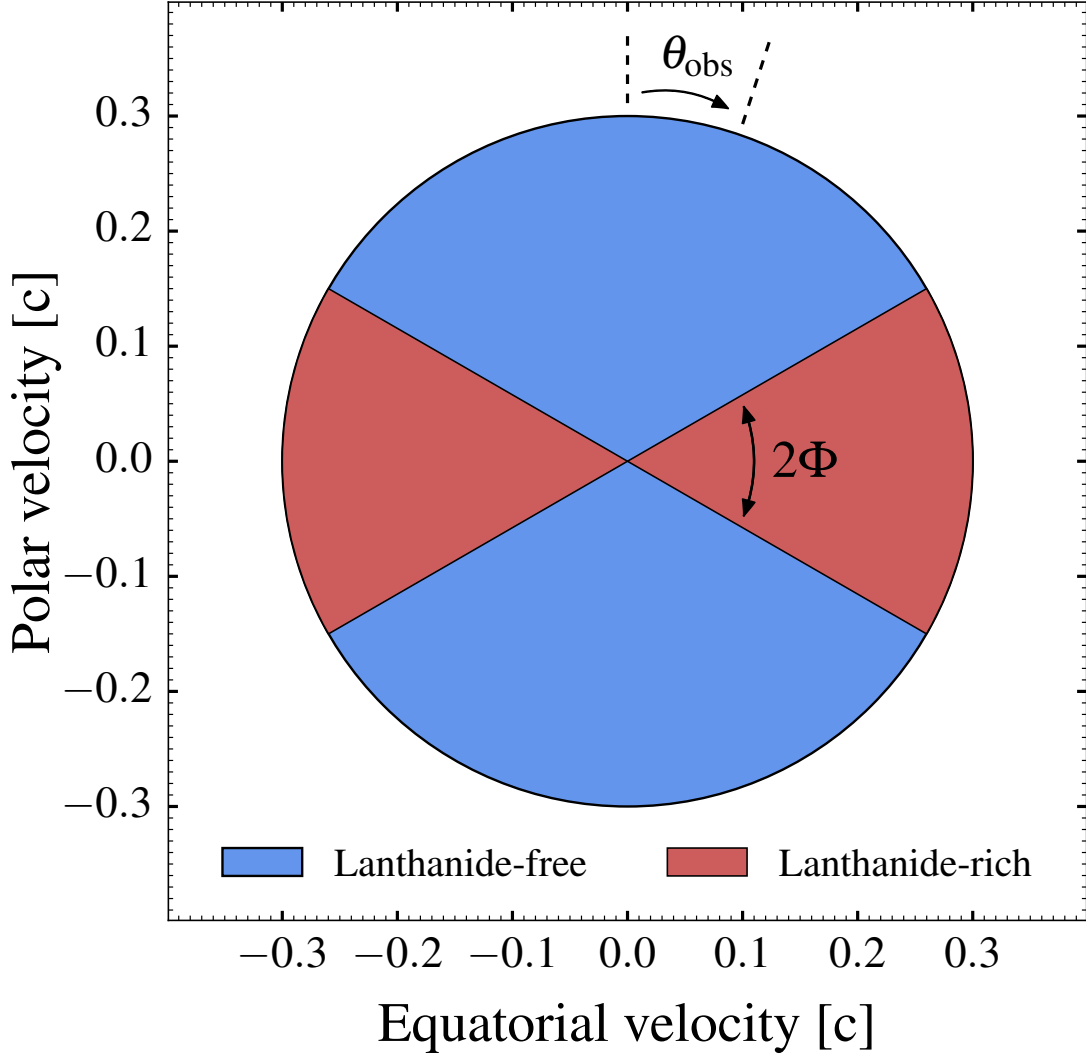


Figure 1: Sketch of the fiducial kilonova model used in this work. A meridional cross section of the ejecta is shown. Two ejecta components are adopted: a first component distributed around the equatorial plane and characterized by lanthanide-elements opacities (“lanthanide-rich component”, in red) and a second component at higher latitudes characterized by lower opacities (“lanthanide-free component”, in blue). These are grossly responsible for the “red” and “blue” components introduced to model the observed spectra of AT 2017gfo^{7,8}. The half-opening angle of the lanthanide-rich region is set to $\Phi = 30^\circ$. Polarization signals are calculated as a function of viewing angle θ_{obs} , where $\cos \theta_{\text{obs}} = 1$ corresponds to the polar direction.

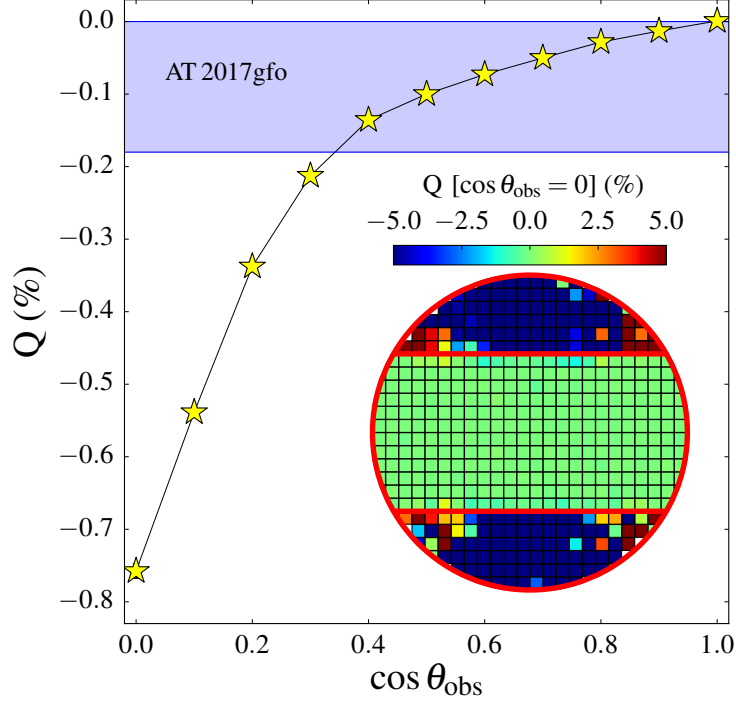


Figure 2: Predicted linear polarization at 1.5 days and at 7000 \AA as a function of the viewing angle of the system, θ_{obs} (yellow stars). Uncertainties are smaller than the symbol size. The Stokes parameter Q expresses the difference in intensity between the electric field components along the vertical and horizontal direction. The blue shaded area marks the range of polarization estimated for AT 2017gfo after removing the interstellar polarization contribution (see Methods - Upper limits to AT 2017gfo intrinsic polarization) from the signal detected in ⁵. The very small level of polarization in AT 2017gfo is consistent with a system observed within 65 degrees from the polar axis ($\cos \theta_{\text{obs}} \gtrsim 0.4$), a value that is less restrictive but consistent with independent estimates from the literature^{1,7,40–42}. The inset shows contributions to Q for an equatorial viewing angle ($\cos \theta_{\text{obs}} = 0$), with the red horizontal lines delimiting the lanthanide-rich ejecta component (cf Fig. 1) and the size of each pixel equal to $0.025 c$. Contributions from regions between the horizontal red lines are preferentially depolarized by bound-bound interactions in the lanthanide-rich component (green, $Q \sim 0$) while those at higher latitudes are preferentially polarized by electron scattering (blue, $Q < 0$) in the lanthanide-free component.

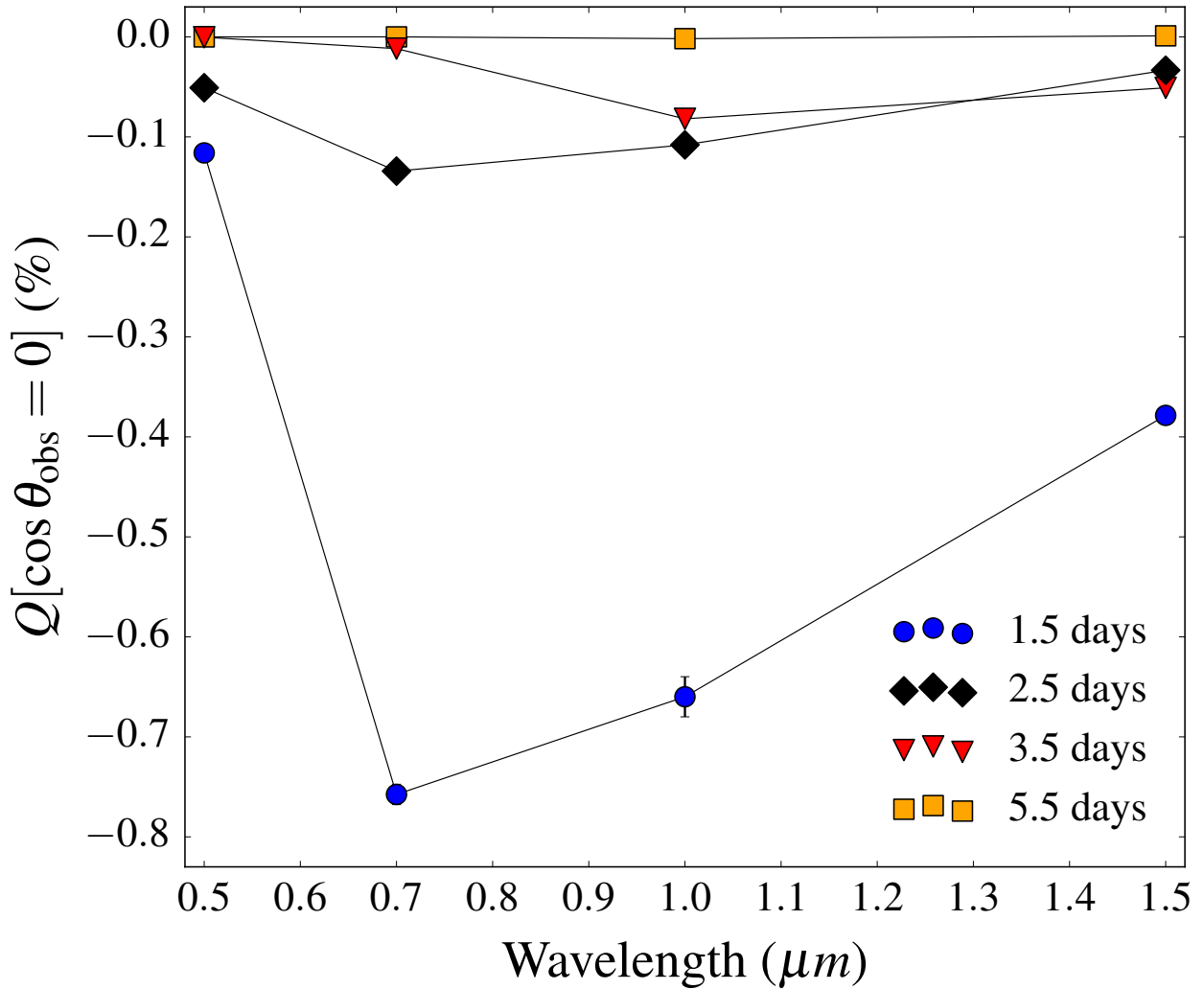


Figure 3: Linear polarization Q for an equatorial viewing angle ($\cos \theta_{\text{obs}} = 0$) at different wavelengths and epochs. Wavelengths are chosen to match several often used broadband astronomical filters. The best chances for a positive detection are predicted around 7000 \AA (R band) and at relatively early epochs (1 – 2 days from the merger). The polarization in the optical becomes negligible from 2 – 3 days after the merger, thus providing a powerful way to characterize the time-independent interstellar polarization in AT2017gfo and future kilonova events. Uncertainties are smaller than the symbol size for most datapoints.

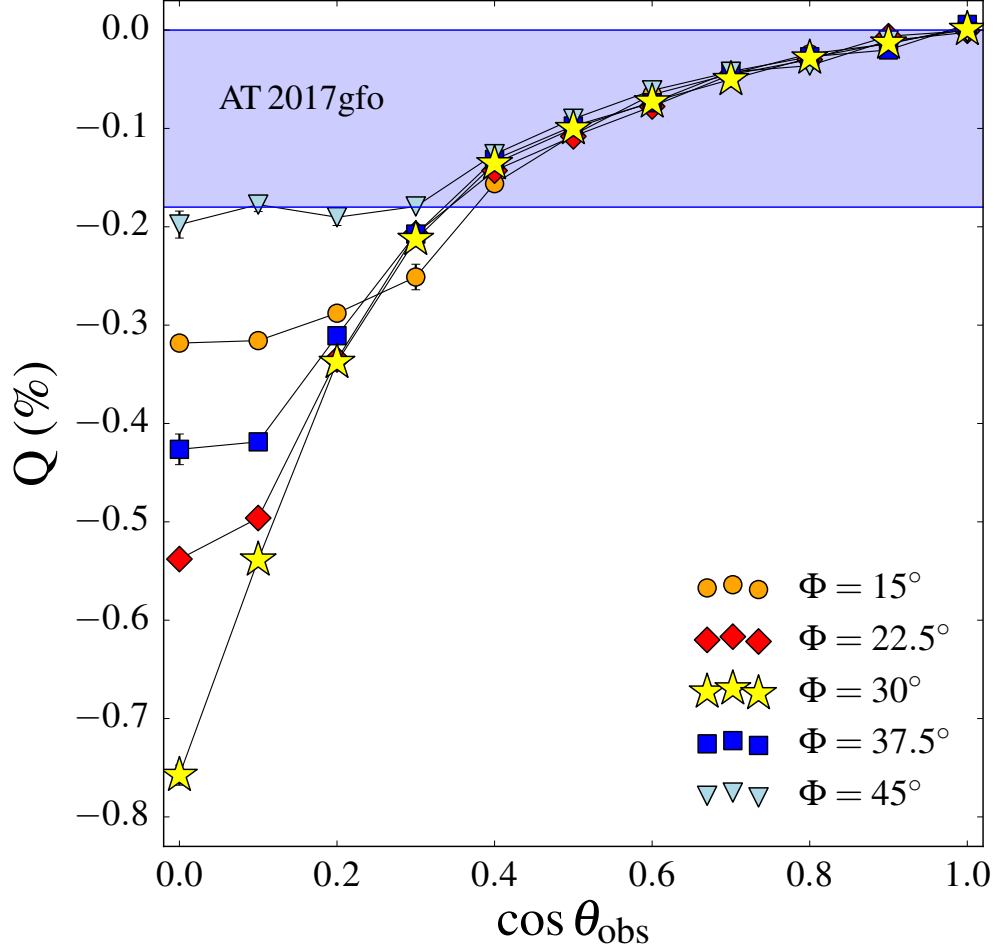


Figure 4: Impact of the half-opening angle of the lanthanide-rich ejecta, Φ , on the polarization signal predicted at 7000 \AA and 1.5 days after the merger. The blue shaded area marks the range of polarization estimated for AT 2017gfo after removing the interstellar polarization contribution (see Methods - Upper limits to AT 2017gfo intrinsic polarization) from the signal detected in ⁵. At low inclinations ($\cos \theta_{\text{obs}} \lesssim 0.2$), the largest polarization degree is found for $\Phi = 30^\circ$, corresponding to the lanthanide-rich ejecta covering half of the full solid angle ($\Delta\Omega = 2\pi$). Similar polarization levels are found for viewing angles closer to the polar direction ($\cos \theta_{\text{obs}} \gtrsim 0.4$). The plot highlights how constraints derived in this study for the inclination of AT 2017gfo, $\cos \theta_{\text{obs}} \gtrsim 0.4$, are rather insensitive to the choice of Φ . Uncertainties are smaller than the symbol size for most datapoints.

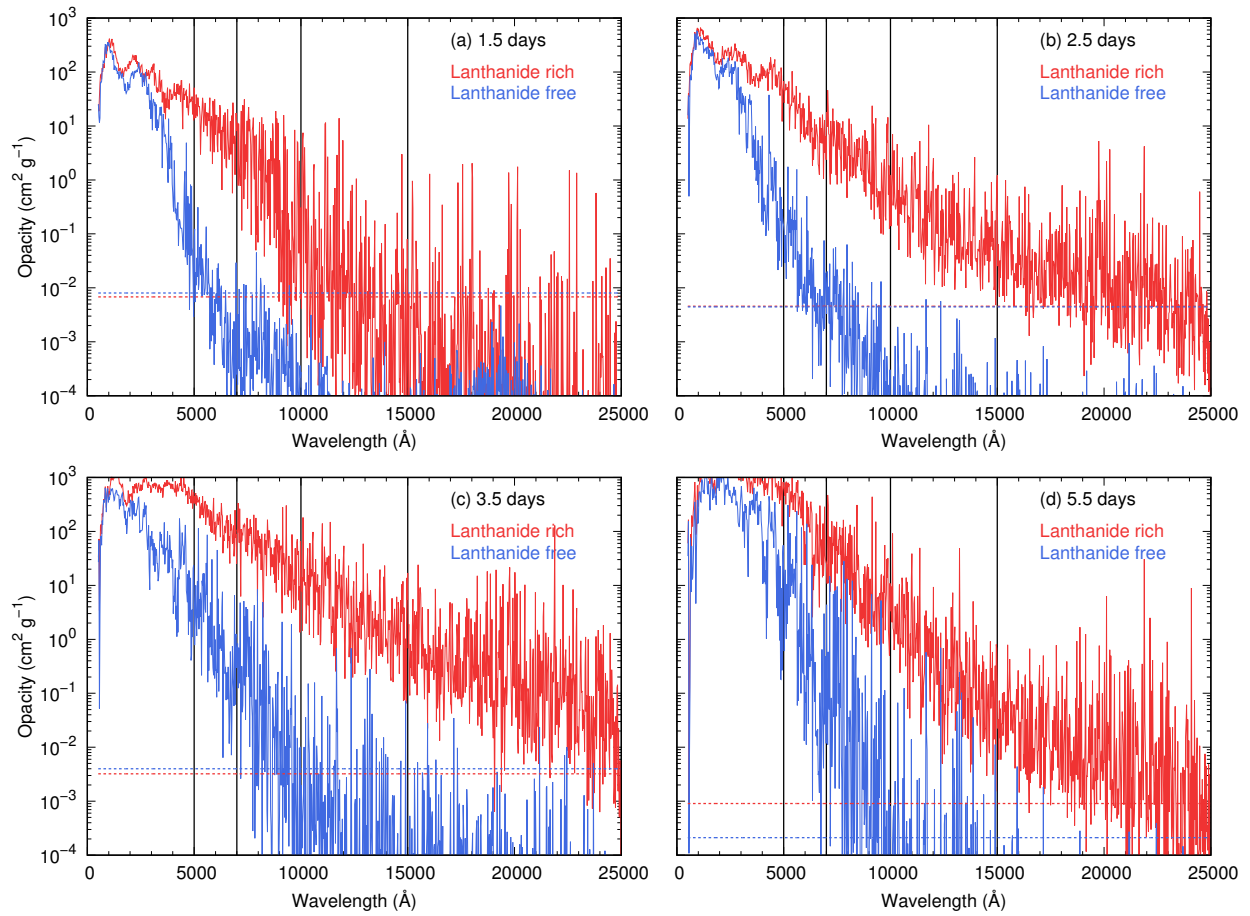


Figure 5: Opacities for the lanthanide-free component at high latitudes (blue) and lanthanide-rich component at low latitudes (red) at 1.5 (panel a), 2.5 (b), 3.5 (c) and 5.5 (d) days after the merger. Solid lines refer to bound-bound opacities, while horizontal dashed lines to electron scattering opacities. Bound-free and free-free opacities are neglected as they are between ~ 5 and 12 orders of magnitudes smaller than electron scattering and bound-bound opacities at epochs and wavelengths (5000, 7000, 10 000 and 15 000 \AA , vertical lines) considered in this work.

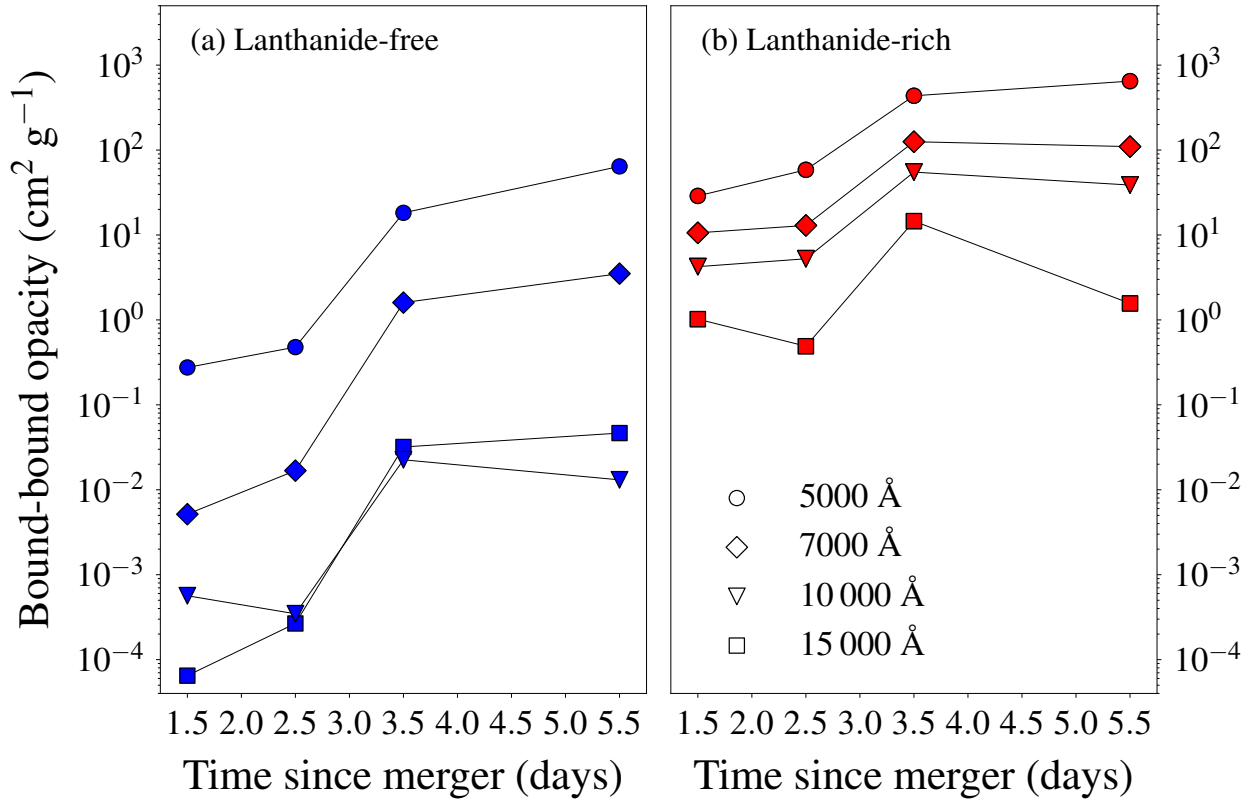


Figure 6: Bound-bound opacities used in the simulations as a function of time since merger. Opacities are shown for lanthanide-free (panel a) and lanthanide-rich (panel b) components at wavelengths (5000, 7000, 10000 and 15000 Å) and epochs (1.5, 2.5, 3.5, 5.5 days) considered in this work. Values are calculated by averaging bound-bound opacities of Fig. 5 over a range of $\Delta\lambda = 500$ Å centered at the desired wavelengths.